17

Dynamic Physical Reliability in Application to Photonic Materials

Dov Ingman[a], Tatiana Mirer[b], and Ephraim Suhir[c]

[a]*Technion, Israel Institute of Technology, Haifa, Israel*
[b]*Technion, Israel Institute of Technology, Quality Assurance and Reliability, Haifa, Israel*
[c]*University of California, Santa Cruz, CA, University of Maryland, College Park, MD, and ERS/Siloptix Co., Los Altos, CA, USA*

17.1. INTRODUCTION: DYNAMIC RELIABILITY APPROACH TO THE EVOLUTION OF SILICA FIBER PERFORMANCE

The widespread application of fiber light-guides in optical communication systems and in diverse physical field transducers has enhanced interest in their mechanical reliability (see, for instance, [1,28,35,36]). The latter is defined as the probability of the fiber rupture or cracking under load.

A defect-free silica glass fiber possesses higher strength than even a steel wire of the same diameter; however, a minimal contact of the silica core surface with a hard object or even with a dust particle gives rise to microcracks. These begin growing rapidly in the presence of moisture and on the application of a tensile load. As a result, the tensile strength of the silica fibers turns out to be much lower than its theoretical strength.

Silica glass is a brittle material, i.e., is a material that does not exhibit any appreciable plasticity under deformation. Reliability prognostication of the mechanical behavior of such materials causes significant challenges [1,24,29,35]. This is because of the high strength scatter and the absence of any preliminary "symptom" (such as, say, plastic deformation) preceding rupture.

As the microcracking process is random, the most suitable model for describing the fiber strength should be statistical [21,22,25,30,34]. The existing fracture mechanics based predictive models use mathematical/mechanical apparatus without any reference to the statistics of the crack propagation and statistical characteristics of the time to failure [23,26,27, 32,33]. The traditionally used combinations of two Weibull distributions are essentially static and do not account for the dynamic nature of the material strength deterioration, which is typically inherent to material under an external or an internal load. The equation for the evolution of the reliability distribution function, described in Section 17.1.1, is applied in our analysis in conjunction with a proposed new physical model of strength deterioration. This model is intended to adequately describe the process of damage accumulation.

The mechanism of the propagation of surface flaws in silica optical fibers is governed by a combination of stress, moisture, temperature, and time. In Section 17.1.2 we suggest a predictive model for time-to-failure when the material is subjected to the action of a three-dimensional mechanical-temperature-humidity load. The model is based on the dynamic physical damage accumulation model described in Section 17.1.1.

The statistical distribution of the tensile strength of optical silica fibers exhibits bimodality. This phenomenon is usually attributed to two different types of flaws in the fiber material. Section 17.1.3 addresses the effect of the bimodality based on an approach that uses the suggested model. We introduce a new micromechanical model of damage accumulation. This model is related to the parameters of the damage evolution equation.

17.1.1. Dynamic Physical Model of Damage Accumulation

The recently proposed dynamic reliability theory for the damage accumulation processes [2,3] is based on the energy aspect of the stress/element interaction. This interaction is reflected in the transitions between the consequent damage states represented by a Markovian stochastic process. The Markovian process describes the dynamic evolution of the system in terms of the change in its reliability distribution function over the range of sequential damage states. The interaction of the loaded specimen with the environment is treated in our approach as a combination of two distinct types. The first type is of a "potential" character determined by the elastic energy of the specimen as a whole, or, alternatively, by the probability density of the elastic energy distribution in the material. This probability is characterized by the likelihood of the material (its ability) to return to the previous damage state after the removal of the applied stress. The second type is of a "local" nature, which is characterized by the energy-dissipative mechanisms of microstructural rearrangement during the deformation process. This type of the interaction of the loaded specimen with the environment is always accompanied by the energy consumption and local structural changes, such as initiation and propagation of microvoids and microcracks. The accumulation process is considered as one of transfer by transition. This process is characterized by elastic potential curves that correspond to different damage states of the material. The transitions are due to the intrinsically stochastic mechanisms of formation and growth of micro-cavities and microcracks: vacancy diffusion in dislocation annihilation, climb-up, etc. Such transitions require local delivery of sufficient energy for the work of rupture of atomic bonds and separation of the atomic planes.

At each damage state, N, the elastic energy per unit volume for a simple tensile load is:

$$U_N = \frac{E_N \cdot \varepsilon^2}{2 \cdot (1 - 2 \cdot \nu_N)}, \tag{17.1}$$

where E_N is Young's modulus of the material at the state N, ε is the strain and ν_N is Poisson's ratio for state N. Figure 17.1 shows a series of elastic potential curves. Although the exact shape of a particular curve depends on temperature, the material microstructure, etc., its general features are assumed to represent a wide range of time-dependent processes of strength deterioration under stress loading.

Transition to the state N involves dynamic relaxation of the material to the state of mechanical equilibrium corresponding to this state. The maximum slope of the relevant

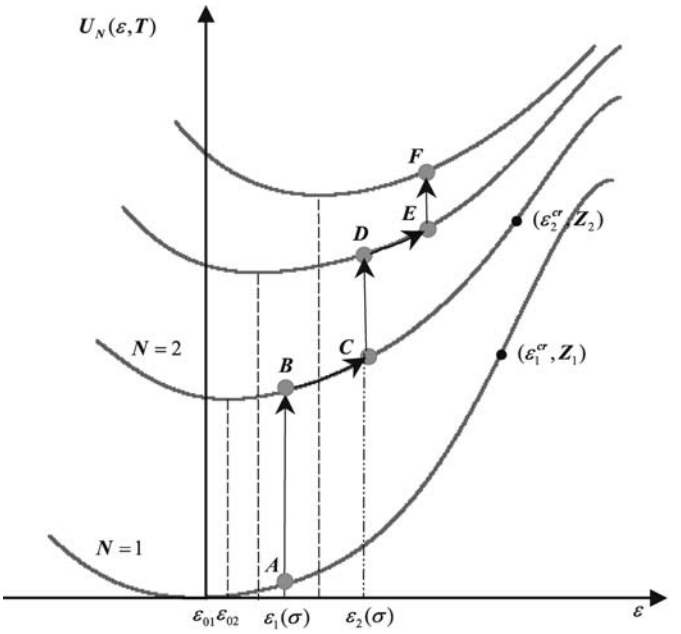

FIGURE 17.1. Elastic energy potential representation of damage accumulation process [1].

curve represents the corresponding maximum material strength Z_N, which decreases as the number N increases. The failure criterion in this model reads:

$$Z_{N_{cr}} = \sigma(t). \tag{17.2}$$

Figure 17.2 illustrates the implementation of this failure criterion through the material's stress–strain diagrams.

The state transitions are induced by fluctuations in the local factors of the element-stress interaction. Since the transition rate function, $\omega(N', N)$, depends on the onset of local fluctuations with sufficient amounts of energy, the transition rate function can be written, according to the theory of statistical fluctuations, as

$$\omega(N', N) = \omega_0(N', N) \cdot \exp[-\Delta S(N', N)]. \tag{17.3}$$

Here $\omega_0(N', N)$ should be viewed as a (temperature and damage state dependent) material constant, and $\Delta S(N', N)$ is the entropy change associated with the transition between the states N' and N with the corresponding microstructural rearrangement.

The damage accumulation rate, $\dot{N}$, is determined as:

$$\begin{aligned}
\dot{N} &= \dot{N}_+ + \dot{N}_- = 2\omega_0 \cdot \sinh\left(\frac{\Delta \cdot \sigma}{\rho \cdot R \cdot T/A}\right) \cdot \exp\left(-\frac{Q}{\rho \cdot R \cdot T/A}\right), \\
\dot{N}_+ &= \omega_0 \cdot \exp\left(-\frac{Q - \Delta \cdot \sigma}{\rho \cdot R \cdot T/A}\right), \\
\dot{N}_- &= \omega_0 \cdot \exp\left(-\frac{Q + \Delta \cdot \sigma}{\rho \cdot R \cdot T/A}\right).
\end{aligned} \tag{17.4}$$

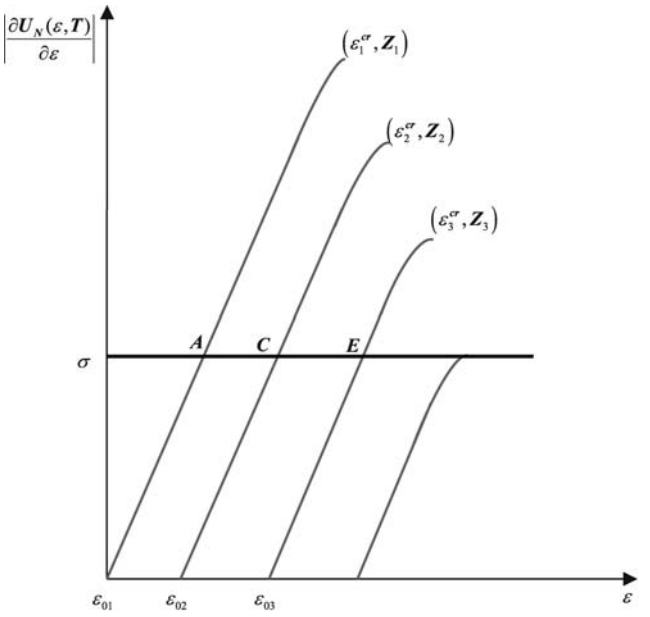

FIGURE 17.2. Stress-strain diagram representation of damage accumulation process [1].

Here $\dot{N}_+$ is the damage accumulation rate, $\dot{N}_-$ is the recovery rate, ρ is the material density; A is the atomic weight; R is the gas constant, Q is the activation energy represented by the ordinate increment, and Δ is the abscissa increment.

17.1.1.1. Reliability Distribution Function The reliability distribution function (RDF) [4] is defined as the probability density function, $r(x,t)$, for finding an element functioning at the moment of time t and having strength in the interval $(x, x+dx)$, x being a generalized strength parameter. The conventional reliability function, $R(t)$, can be expressed through the RDF as follows:

$$R(t) = \int_{(x)} r(x,t)dx. \tag{17.5}$$

The integral of the RDF over the strength space expresses the probability of finding an element functioning at time t, while being on a non-failed strength level. The Smoluchowski's probability of transition from the strength level, x, to a weaker state, x', should satisfy the normalization condition:

$$\int_{x' \le x} P(x \to x')dx' = 1. \tag{17.6}$$

The rate of change of the RDF is determined by the rates of three processes:

(1) The failure rate at the strength level x: $\lambda(x,t) \cdot r(x,t)$, where $\lambda(x,t)$ is the rate of events with a stress level above the element strength, x, and leading, therefore, to the element's failure;
(2) the rate of the strength deterioration: $\omega(x,t) \cdot r(x,t)$, where $\omega(x,t)$ is the rate of events below the element strength at time t;

(3) the integral rate of transition to the strength level x from the higher strength state x':

$$\int_{x'>x} \omega(x',t)\,p(x' \to x)r(x',t)dx'. \tag{17.7}$$

While the first two terms in (17.7) tend to reduce the RDF, the last term tends to increase it. The transfer equation for the RDF can be written therefore in the following form:

$$\frac{\partial r(x,t)}{\partial t} = -[\lambda(x,t) + \omega(x,t)] \cdot r(x,t) + \int_{x'>x} \omega(x',t)\,p(x' \to x)r(x',t)dx' + \delta(t) \cdot r(x,t). \tag{17.8}$$

The function $r(x,t)$ in the last term accounts for the initial values $r(x,0)$, and should satisfy the requirement:

$$R(0) = \int_{(x)} r(x,0)dx = 1. \tag{17.9}$$

The assumption that x_0 is the initial strength distribution of the "virgin" undamaged fiber, so that $r(x,0) = \delta(x - x_0)$, does not entail any lack of generality, since the solution obtained on this basis can serve as a Green function for any other initial distribution $f(x) = r(x,0)$. In such a case, $r(x,t)$ can be found as the following convolution:

$$r(x,t) = \int_0^\infty r_{x_0}(x',0) \cdot f(x - x')dx'. \tag{17.10}$$

The simplified model for the transfer function $p(x' \to x)$ is chosen in the following form:

$$p(x' \to x) = \beta \cdot \frac{x^{\beta-1}}{(x')^\beta}. \tag{17.11}$$

17.1.2. Impact of the Three-Dimensional Mechanical-Temperature-Humidity Load on the Optical Fiber Reliability

As it has been mentioned above, the basic factor of crack propagation in silica glass is the combination of stress, moisture, temperature, and time [16,18]. The Equation (17.4) represents the damage accumulation rate as a function of stress and temperature. Accordingly, the time to failure dependence on stress and temperature should be exponential as well. Assuming that for a relatively high load the recovery part is negligible, time to failure can be represented as follows:

$$t = t_0 \cdot \exp\left(-\frac{Q - \Delta \cdot \sigma}{\rho \cdot R \cdot T/A}\right). \tag{17.12}$$

TABLE 17.1.
Activation energy (eV) for some type of fibers for 45% and 100% humidity.

Sample 1	Stress, GPa					
	4.84		5.05		5.28	
	RH = 45%	RH = 100%	RH = 45%	RH = 100%	RH = 45%	RH = 100%
	3.896	3.88	3.896	3.88	3.891	3.868
Sample 2	Stress, GPa					
	4.55		4.74		4.94	
	RH = 45%	RH = 100%	RH = 45%	RH = 100%	RH = 45%	RH = 100%
	3.827	3.721	3.826	3.723	3.826	3.728
Sample 3	Stress, GPa					
	4.65			4.84		
	RH = 45%	RH = 100%		RH = 45%		RH = 100%
	3.755	3.566		3.755		3.564
Sample 4	Stress, GPa					
	4.65			4.84		
	RH = 45%	RH = 100%		RH = 45%		RH = 100%
	3.899	3.886		3.899		3.886

We proceed from the idea that the main reason of a slow crack growth is humid environment. Elevated relative humidity (RH) decreases the activation energy. With this in mind, Equation (17.12) could be written as:

$$t = t_0 \cdot \exp\left(-\frac{Q(\mathrm{RH}) - \Delta \cdot \sigma}{\rho \cdot R \cdot T/A}\right). \tag{17.13}$$

Here the function $Q(\mathrm{RH})$ is assumed to be linear, with intercept (0% humidity) equal to sublimation energy of the material. Table 17.1 shows the levels of the activation energy, which were evaluated for different fiber types and different loads for 45% and 100% humidity. It is clear that the activation energy does not depend on the applied load, but depends only on the relative humidity (RH) and the fiber type. Humid environments reduce the activation energy and therefore accelerate the crack grows and, consequently, the process of the damage accumulation.

17.1.3. Effect of Bimodality and Its Explanation Based on the Suggested Model

The standard analysis of the strength data is based on the Weibull distribution:

$$F(x) = 1 - \exp\left[-\left(\frac{x}{\theta}\right)^{\eta}\right], \tag{17.14}$$

where θ is the scaling parameter, η is the shape parameter, and x is strength. The function $\ln[-\ln(1 - F(x))]$ is a linear function of x, with η as a slope and $-\eta \cdot \ln(\theta)$ as an intercept of the line [34].

The strength distribution for optical fibers is usually represented on a Weibull scale. According to most references and the authors' own experimental data, the obtained slope

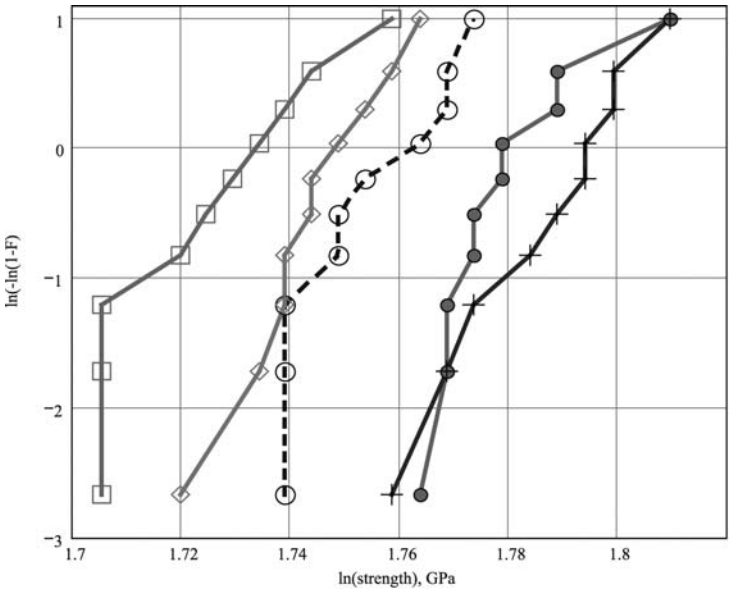

FIGURE 17.3. Examples of optical fiber strength distribution (Weibull Plot).

(the shape parameter in the Weibull distribution) comprises, actually, two different components [5]. Some examples of the strength probability distribution (cumulative distribution function) are shown in Figure 17.3. If the application of the Weibull distribution is justified, i.e., if this distribution adequately reflects the physics of rupture, then the plots should be straight lines. Deviations from such straight lines cannot be explained by statistical uncertainties, but clearly indicate a need for corrections in the model itself. The S-shape line behavior of the test data indicates that the statistical strength distribution could be bi- or even multimodal.

Most references [6,7] assume that bimodality can be explained from the standpoint of the interaction of the "low strength" due to the "external" defects (caused by various mechanical and chemical factors), and "high strength" which is due to various "internal" defects, such as production process defects, thermal fluctuations etc. Consequently, some researchers claim that the Weibull distribution is, in general, unsuitable. They suggest a superposition of two such distributions with two different shape- and scale parameters. Note that, unlike the "regular" Weibull distribution, the bimodal Weibull model is, actually, a *five*-parameter distribution.

In our concept, the two-slope phenomenon in the fiber strength distribution is explained not as an intrinsic feature of the fibers, but rather as a combination of the original strength distribution of the "virgin" (undamaged) material ("strong mode") and the secondary distribution ("weak mode"), developed in the process of damage accumulation under an external and/or internal load. The high-slope portion describes the "original," "young," "non-aged" strength distribution and the low-slope portion of the distribution describes the performance of the damaged population [8].

The tensile test [9] is viewed as a suitable test valid for comparative analysis of the initial and the post-loading distributions of the fiber. In these experiments, 5 m long silica glass fiber specimens of outer diameter 300 μm were divided into five groups. We prepared and tested at least 60 specimens. The first group was subjected to the standard test

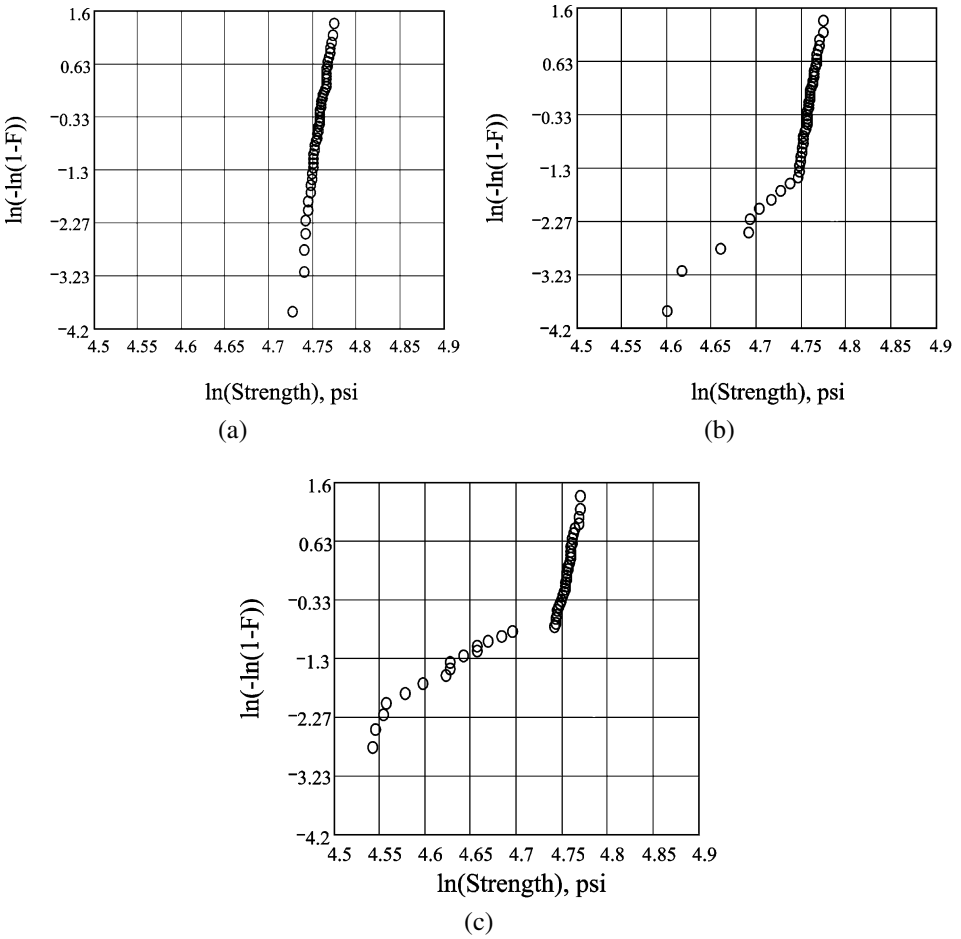

FIGURE 17.4. Strength Weibull plot of (a) undamaged fibers; (b) fibers exposed to low load dose; (c) fibers exposed to high load dose.

(with a constant strain rate), and the other specimens were preliminarily subjected to different "doses" of load, and only after that were subjected to the tensile test. Figure 17.4(a) shows the Weibull chart of the initial fiber. It is clear that the distribution is unimodal. The post-loading distributions begin to look like bimodal [Figures 17.4(b), 17.4(c)] and exhibit several behavioral patterns. Initially, the fiber strength can be described by a homogeneous high-slope distribution with a small standard deviation [Figure 17.5(a)] and a low-slope component (if any) is integrated into the high-slope distribution as a part of it. Under the applied load the high-slope component retains its initial mean and the standard deviation, but the low-slope component becomes more strongly pronounced [Figure 17.5(b)]. Here is the explanation of this phenomenon.

The population of fibers with the low strength increases because of the damage accumulation process. The low-slope part represents the strength distribution of the damaged parts and their source in the initial fibers (high-slope distribution). Area under the low-slope distribution increases at the account of the area of the high-slope part as a result of additional loading [Figures 17.5(b), 17.5(c) and 17.5(d)]. By the end of the process the part

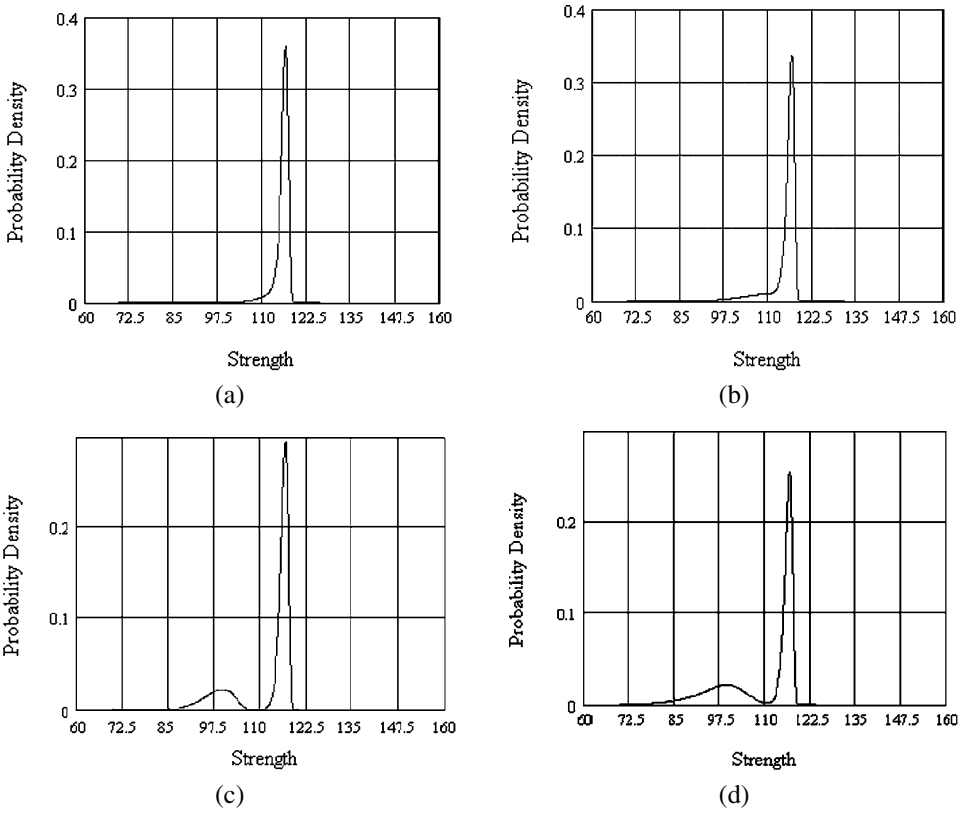

FIGURE 17.5. Strength distribution of (a) undamaged fiber; (b) fibers exposed to low load dose; (c) fibers exposed to medium load dose; (d) fibers exposed to high load dose.

of fibers with the initial strength will vanish (due to the transition to the subpopulation with lower strength and, less probable, due to failure), and only the low-slope distribution with a small mean and a large standard deviation will remain.

In characterizing the damage accumulation process in brittle solids, many researchers agree that such a process starts with the random formation of numerous micron-sized cracks (microcracks) throughout the solid [10–12,17,20]. The size of these microcracks is comparable to that of the defects that are initially present in the "virgin" unloaded material. When the characteristic distance between the adjacent microcracks (correlation length) reduces to a certain threshold value, the microcracks begin to coalesce, forming microcrack clusters. One of these clusters eventually develops into a macroscopic crack, which continues growing until the solid ruptures [31]. As to the time scale, the first stage of the damage accumulation process is, on the average, much longer than the second stage, while the last (third) stage is usually very short compared to the previous stages. The strength deterioration at the first stage is mainly determined by a typical size of the microcrack and is approximately constant (within the statistical "noise").

In the evolution Equation (17.8) it is assumed that the load on the fiber is relatively small, i.e., $x \gg \sigma$, and, accordingly, the failure rate is negligible. The governing Equation (17.8) reduces to

$$\frac{dr(x,t)}{dt} = -\omega(x,t) \cdot r(x,t) + \int_{x'>x} \omega(x',t) \cdot p(x' \to x) \cdot r(x',t) dx'. \tag{17.15}$$

The rate, $\omega(x,t)$, of the strength deterioration at the first stage of the damage accumulation process ($x = x_0$) is merely the inverse of the mean stage duration and, therefore, may be by several orders of magnitude lower than that at the second stage ($x < x_0$). The second stage is generally a time- and strength-dependent process controlled by the frequency of the microcracks formation in the vicinity of a cluster. In many practical situations, however, it may be approximated by a constant [10,12,13]. As the third stage is negligibly short in time, the transition rate may be approximated for our purposes as follows:

$$\omega(x,t) = \begin{cases} \omega, & x < x_0 \\ \Omega, & x = x_0 \end{cases}, \quad \omega \gg \Omega. \tag{17.16}$$

The strength transition probability, $P(x \to x')$, during the second stage of damage accumulation can be estimated based on the following reasoning. Consider a solid that comprises both discrete microcracks and microcrack clusters. The strength of such a solid is defined by the size of the largest cluster. Let us enclose the largest cluster into a 3D lattice such that its links are small relatively to a typical microcrack [see Figure 17.6]. The strength of the solid is related to the size of the largest cluster as [12,14]

$$x = B \cdot N^{-v}, \tag{17.17}$$

where B and v are positive material constants, and N is the number of the lattice sites in the cluster. We attribute the growth of a cluster to thermal-fluctuation formation of new microcracks in the vicinity of the cluster. The probability of nucleation of a new microcrack

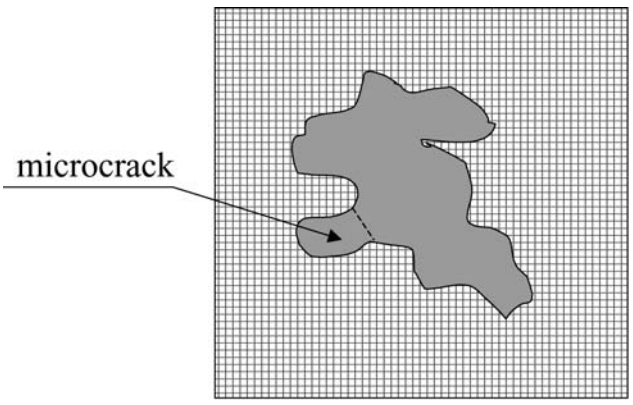

FIGURE 17.6. The largest microcracks cluster circumscribed by a percolation lattice. The lattice shown is a 2D lattice, but generally it can be 3D. The lattice links are small relatively to a typical microcrack size.

in the vicinity of the cluster, i.e., the probability of N increasing by increment ΔN, is then given by

$$P(N \to N + \Delta N) \sim \exp\left(-\frac{\Delta S}{k_B \cdot T}\right), \tag{17.18}$$

where k_B is the Boltzmann's constant, T is the absolute temperature, and S is the configuration entropy. It can be shown that for $N \gg 1$ and $\Delta N \ll N$, the entropy increment is approximately $\Delta S \approx \Delta N/N$, leading to

$$P(N \to N + \Delta N) \approx A \cdot \exp\left(-C \cdot \frac{\Delta N}{N \cdot k_B \cdot T}\right). \tag{17.19}$$

From (17.17) and (17.19) we have

$$P(x \to x') = A \cdot \exp\left(-\frac{v \cdot B \cdot C}{k_B \cdot T} \cdot \frac{x - x'}{x}\right). \tag{17.20}$$

This expression, for $x - x' \ll x$, is identical to the empirical relation (17.11) in Section 17.1.1. Indeed,

$$\exp\left(-\beta \cdot \frac{x - x'}{x}\right) = \left[\exp\left(\frac{x' - x}{x}\right)\right]^{\beta} \approx \left(1 + \frac{x' - x}{x}\right)^{\beta} = \left(\frac{x'}{x}\right)^{\beta}. \tag{17.21}$$

Therefore, the empirical parameter β is given by

$$\beta = \frac{v \cdot B \cdot C}{k_B \cdot T}. \tag{17.22}$$

The parameter B is proportional to the material's fracture toughness [12,13,19]: the tougher the material, the higher the β value and the narrower is the transition probability distribution. The form (17.11) of the transition probability, although approximate, is nevertheless preferable it since (as is shown in the next section), it enables one to proceed with an analytical solution to the evolution Equation (17.15). The corresponding single-parameter transition probability density function can be found as

$$p(x \to x') = (\beta + 1) \cdot \frac{(x')^{\beta}}{x^{\beta+1}}. \tag{17.23}$$

17.1.3.1. Time Behavior of the Reliability Distribution Function [8] The Laplace transform

$$\tilde{r}_{x_0}(x, s) = \int_0^{\infty} \exp(-s \cdot t) r_{x_0}(x, t) dt \tag{17.24}$$

of the solution of Equation (17.8) with the obtained relationships (17.16) and (17.23) has the following form:

$$\tilde{r}_{x_0}(x, s) = (\beta + 1) \cdot \frac{\Omega}{(\Omega + s) \cdot (\omega + s)} \cdot \frac{1}{x} \cdot \left(\frac{x}{x_0}\right)^{\frac{(\beta+1)\cdot s}{\omega+s}} + \frac{\delta(x - x_0)}{\Omega + s}. \tag{17.25}$$

In order to obtain the inverse transform in the analytic form, let us consider the first term of the Equation (17.25) and represent it as follows:

$$\frac{(\beta+1)\cdot\Omega}{(\Omega+s)\cdot(\omega+s)}\cdot\frac{1}{x}\cdot\left(\frac{x}{x_0}\right)^{\frac{(\beta+1)\cdot s}{\omega+s}} = \frac{(\beta+1)\cdot\Omega}{x\cdot(\Omega+s)}\cdot\frac{1}{(\omega+s)}\cdot\exp\left[\log\left(\frac{x}{x_0}\right)\cdot(\beta+1)\cdot\left(1-\frac{\omega}{\omega+s}\right)\right]. \tag{17.26}$$

Expanding the exponent into a series we obtain:

$$\tilde{r}_{x_0}(x,s) = \frac{\Omega\cdot(\beta+1)}{x\cdot(\Omega+s)}\cdot\left(\frac{x}{x_0}\right)^{\beta+1} \times\sum_{i=0}^{\infty}\frac{(-1)^i\cdot\omega^i\cdot(\beta+1)^i\cdot\left[\log\left(\frac{x}{x_0}\right)\right]^i}{i!\cdot(\omega+s)^{i+1}}+\frac{\delta(x-x_0)}{\Omega+s}. \tag{17.27}$$

Thus, the inverse transform is the series:

$$r_{x_0}(x,t)=\delta(x-x_0)\cdot\exp(-\Omega\cdot t)+\frac{\Omega\cdot(\beta+1)\cdot\exp(-\Omega\cdot t)}{x}\left(\frac{x}{x_0}\right)^{\beta+1} \times\sum_{i=0}^{\infty}\left\{\frac{(\omega)^i\cdot(\beta+1)^i\cdot\left[\log\left(\frac{x_0}{x}\right)\right]^i}{(i!)^2}\int_0^t(t')^i\cdot\exp(\Omega-\omega)\cdot t'dt'\right\} \tag{17.28}$$

where

$$\int_0^t(t')^i\cdot\exp(\Omega-\omega)\cdot t'dt' = \frac{i!}{(\omega-\Omega)^{i+1}}-\frac{i!\cdot\exp(\Omega-\omega)\cdot t}{(\omega-\Omega)^{i+1}}\sum_{j=o}^{i}\frac{(\omega-\Omega)^j\cdot t^j}{j!}. \tag{17.29}$$

The first term in the obtained distribution (17.28) is the contribution of the "virgin" (original, "undamaged") material and the second term represents the secondary distribution caused by the damage accumulation process. The proportion of the original distribution in the composite structure decreases exponentially with time. Figure 17.7 describes the time evolution of the secondary distribution for a loaded silica fiber. As the central trend of the strength distribution decreases with time, the distribution spreads wider. After a time interval of about $5/\Omega$, the original distribution has practically vanished (no undamaged specimens remain), and the secondary distribution approaches the Weibull curve. The shape parameter of this distribution is governed by the parameter $\beta(15)$, i.e., by the fracture toughness of the material and temperature.

17.1.3.2. Dynamics of the Optical Fiber Strength In order to validate the obtained model let us return to the experiment described at the beginning of this section.

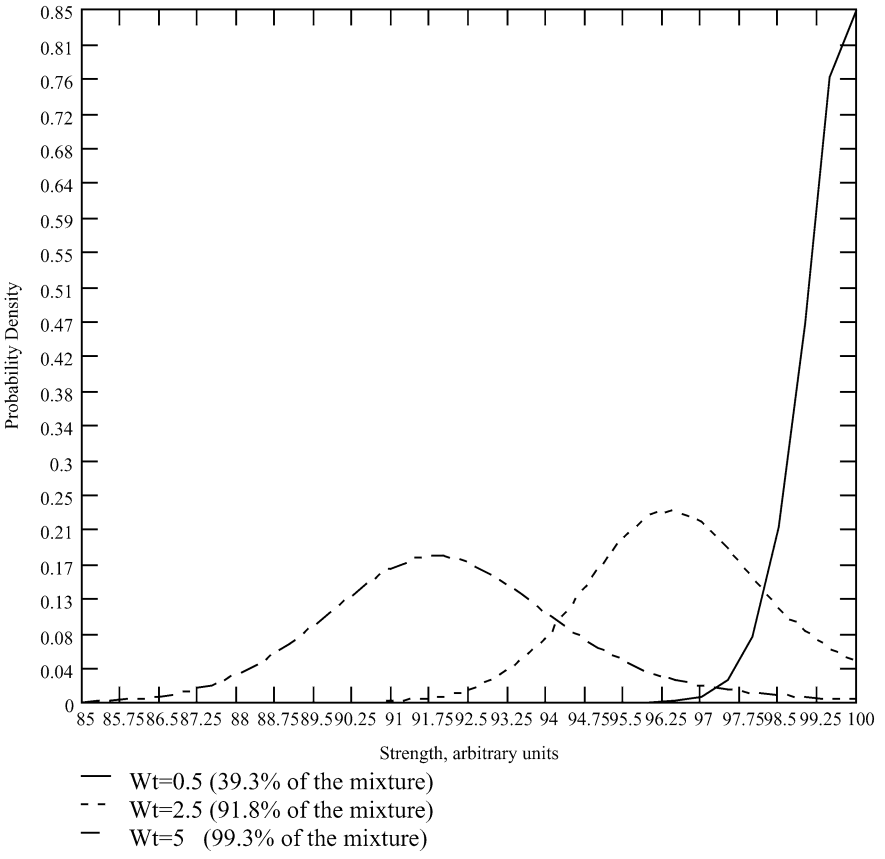

FIGURE 17.7. The Daughter Distribution Dynamics as a solution of the evolution equation.

To estimate the parameters of the predicted distribution (17.28) on the basis of the experimental data, a minimal distance scheme [15] was used. In this scheme, the distance between the empirical Cumulative Distribution Function (CDF) and the analytical one is minimized within the parameter space. The only three parameters in the predicted distribution (17.28) are Ωt, ω and β. The latter two are not supposed to change during the process of damage accumulation. The constancy of the parameters ω and β was used as a convenient condition in the estimation procedure. The delta-function was approximated by a normal distribution, which had an excellent goodness-of-fit for the first-group sample.

Figures 17.8 and 17.9 represent the estimation results for low and high doses of the preliminary stressing, respectively. The agreement between the estimated distributions and experimental results is satisfactory, especially having in mind that only one estimated parameter (Ωt) accounts for the damage dose. For the low preliminary damage the resultant distribution is close to the initial delta-function with a rather small contribution of the "weak mode." For the high preliminary damage the resultant strength distribution exhibits bimodality. Since the initial flaw distribution is apparently the same for all the tested fiber specimens, this bimodality can be explained by the damage accumulated in the preliminarily stressed specimens.

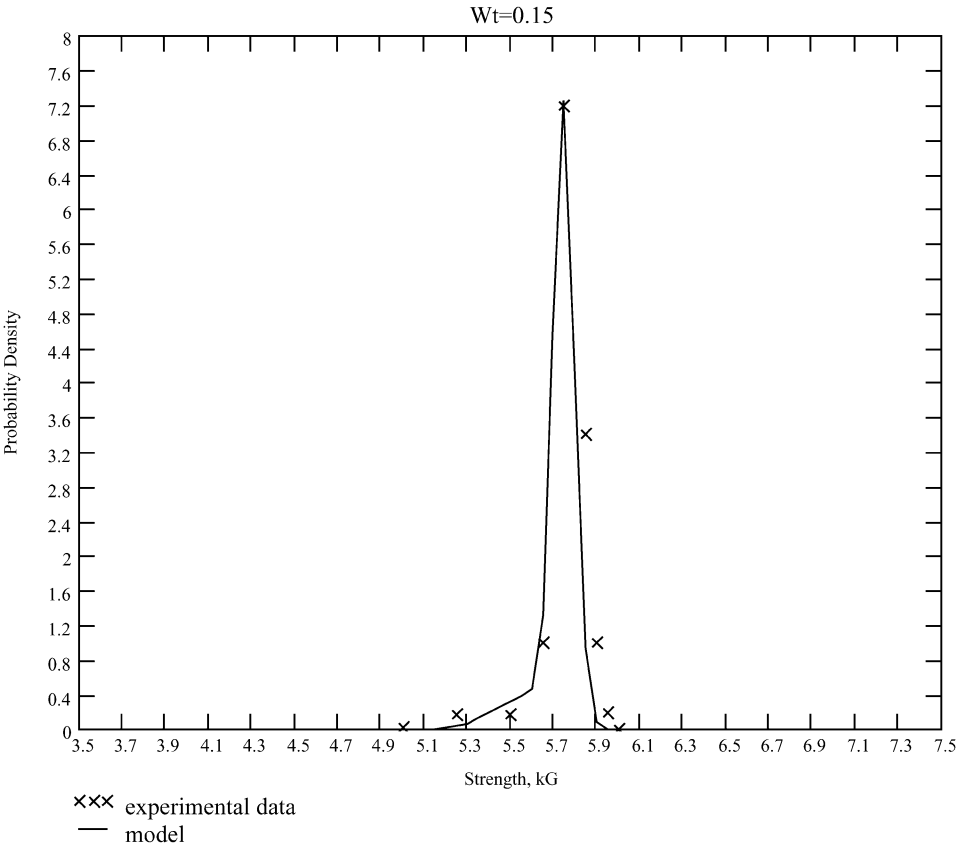

FIGURE 17.8. Experimental strength distribution of optical fibers exposed to a relatively low load dose and the model prediction.

Unlike the traditional approach to statistical modeling of fracture, the present method describes the phenomenon in its dynamics. The proposed approach links the thermal-fluctuation damage events with the corresponding strength deterioration, and thereby establishing an evolution equation of the time-dependent strength distribution whose solution describes the above pattern, which is confirmed experimentally.

The actual strength of the "virgin" material is by several orders of magnitude lower than the theoretical strength calculated on the basis of the material intermolecular forces [10]. This discrepancy is usually attributed to the defects present even in the "virgin" material. Since these defects are not inherent to the material, but formed during the production process and the subsequent use conditions, the proposed approach is quite general and is not limited to the pre-stressed specimens.

The resultant combined distribution has only three parameters, two of which (Ω and ω) characterize the strength deterioration dynamics, and the remaining parameter (β) characterizes the "daughter distribution" shape. The two former parameters are controlled by the rate of the microcrack nucleation, which is governed by the material's fracture toughness and the temperature.

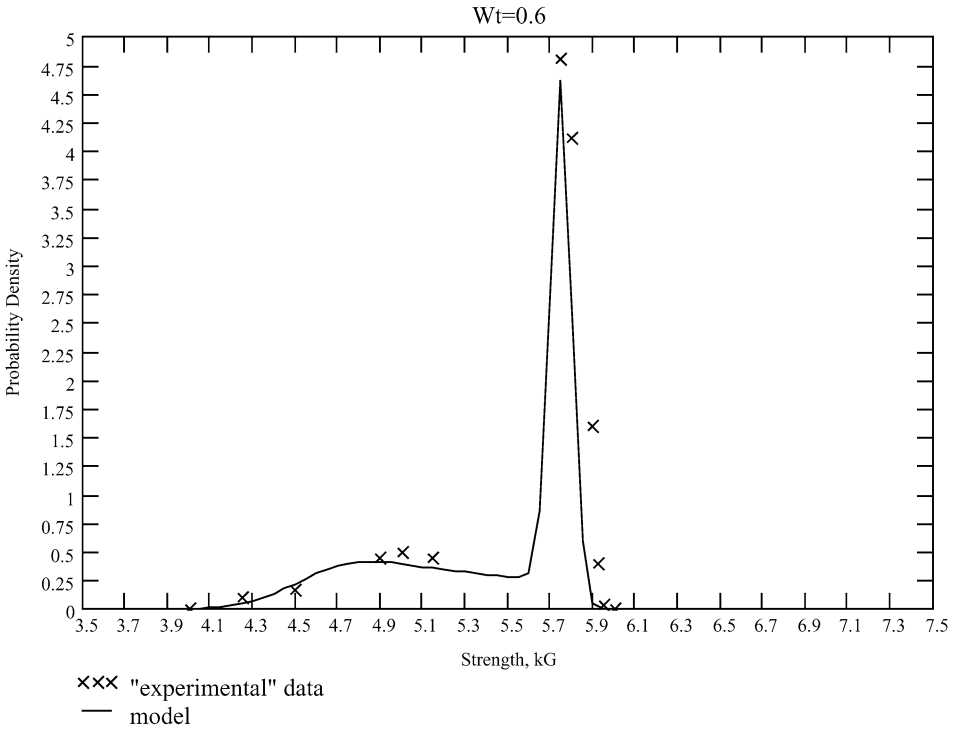

FIGURE 17.9. Experimental strength distribution of optical fibers exposed to a relatively high load dose and the model prediction.

17.2. RELIABILITY IMPROVEMENT THROUGH NPM-BASED FIBER STRUCTURES

17.2.1. Environmental Protection by NPM-Based Coating and Overall Self-Curing Effect of NPM Layers

In a fiber under load, a surface defect acts as a stress concentrator with the maximum stress at its tip, which is the preferential site of moisture attack and rupture of the silica bonds. This causes the defect to spread, and, consequently, the stress to increase in magnitude until the fiber catastrophically fails [28]. Fibers require long-term protection against moisture and oxygen, as well as mechanical and thermal protection. Most existing coatings for optical fiber are polymer-based. These are moisture-sensitive ("non-hermetic"). Although the reliability of polymer coatings has improved considerably during the last decade, it is not as high as necessary for particular applications.

The surface of most polymers is covered with protrusions, typically 0.1–0.3 micron high, their density being of the order of $0.25–1 \times 10^8$ peaks/cm^2 (meaning average spacing of the peaks about 1–2 microns). Under temperature cycles and deformation of the material between the peaks, significant stress concentrations are created in the "gullies" resulting in inter-granular microcracks or pinholes. These defects destroy the continuity of the plastic coating and seem to be the main reason for its permeability to gases.

Nanoparticle-type coating materials (NPM's) could be used to fill the gullies, microcracks and other defects in the plastic. The most important physical property of these materials is their thixotropy, which can be defined as fluidity under stress. This property is

exhibited by some gels that become fluid when stirred or shaken, and revert to a semi-solid state, when stirring or shaking ends. Therefore the same stress that creates or aggravates the defect, makes the NPM less viscous and thus enables it to penetrate (fill in) and "heal" the defect.

Thanks to this effect, plastics no longer have to be designed for a long lifetime (which is usually the main problem). The plastic material may deteriorate: the NPM coating will take care of improving the situation. Another important aspect of the NPM coatings is their moisture-proofing action. The hydrophobic nanoparticles tend to fill in the spaces between the peaks, but do not necessarily follow the profile, so that this part of the film is somewhat flattened. The particles interconnect among themselves and with the coated plastic through the links of the same or a congeneric polymer, whose presence was predetermined in the original coating material. The contents of hydrophobic nanoparticles and of the polymer in the coating material have to correspond to the amounts needed to fill the spaces between the peaks. The characteristic dimension of the spaces between the peaks is about 3–6 Å in a well-packed structure. This narrows tremendously the passages for water molecules. The hydrophilic nanoparticles (one of their functions is to provide the affinity with the coated molecules) form the outer layer of the coating.

The space between the peaks, which are about 0.15 micron in height, is covered by the hydrophobic nanoparticles on both sides of the sheet. Their total volume of these nanoparticles on both sides of the sheet is

$$V_{phob} = \frac{2}{3} \cdot S \cdot h, \tag{17.30}$$

where S is the area of the sheet. The coefficient in front of h is based on the simplifying assumption that the peaks are conical.

Let H be the thickness of the hydrophilic NPM layer. Then,

$$V_{phil} = S \cdot H, \tag{17.31}$$

and, for the same packing density, the concentration ratio between the hydrophilic and hydrophobic nanoparticles is:

$$\frac{V_{phil}}{V_{phob}} = \frac{3 \cdot H}{2 \cdot h}. \tag{17.32}$$

For $S = 1$ m^2, $H = 3$ μm and $h = 1.5 \times 10^{-7}$ m, the volumes of the hydrophobic and hydrophilic parts will be, respectively, $V_{phob} = 10^{-7}$ m^3 (0.07 grams) and $V_{phil} = 3 \times 10^{-6}$ m^3 (2 grams). This correspond to the nanoparticle surface of each kind of $S_{phob} = 20$ m^2 and $S_{phil} \sim 600$ m^2. This amount of hydrophilic particles is able to absorb up to 3 grams of water. This means that even in the case of a plastic with water permeability of 10^{-2} g/m^2/day it will take 300 days for the coating to be completely penetrated, not to mention the "healing" effect of the NPM, nor the another NPM layer on the other side. Due to the extremely low modulus of elasticity of these layers, the flexibility of the systems remains practically unchanged. In some application, it might be a very useful property.

On the other hand, the filling effect of the nanoparticles creates a 3D network of narrow passages with the characteristic width of 3–10 Å, i.e., the one of molecular size (the typical size (diameter) of the water molecule is about 3 Å). If we idealize the packing structure as large balls with the spaces between them filled by smaller balls (Figure 17.10),

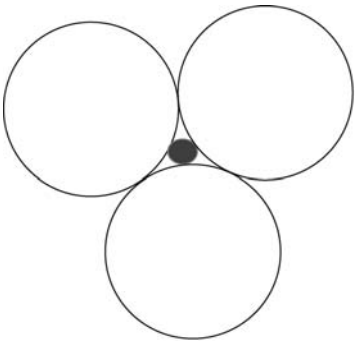

FIGURE 17.10. Packing structure of nanoparticles.

then the smallest remaining spaces between the smallest balls will be about 0.155 of the smallest ball radius. Assuming the smallest nanoparticles to be in the range of 4–10 nm in diameter, the above mentioned passages could be readily evaluated.

This dramatic change in the passage pattern has a drastic effect on the diffusion of oxygen and water molecules through the system. The diffusion coefficient before filling corresponds to that in gases, while after the filling it is expected to be closer to that of solids. The molecule free path lengths in gases are on the order of $\sim$100 nm, while in solids these lengths are on the order of 3–10 nm. This alone is expected to reduce the diffusion coefficient by about 3 orders of magnitude. Another physical mechanism, resulting in a reduced diffusion coefficient is the number of "jumps" per second. In gases, this number is the ratio of the molecule velocity to its free length, while in our, NPM "filled," case, the number of "jumps" per second depends on the activation energy. Our estimation is that this mechanism can add another order of magnitude to the above effect, so that the total reduction in permeability thus being improved by about 4 orders of magnitude.

Thus, the combination of the hydrophilic-hydrophobic layers is expected to provide the necessary protection against the water vapor and oxygen penetrator for an acceptable lifetime.

17.2.2. Improvement in the Reliability Characteristics by Employing NPM Structures in Optical Fibers

In order to compare the mechanical and the environmental characteristics of the NPM-based and "regular" fibers under different loading and environmental conditions, two experiments described below were carried out.

The specimens were obtained from light guides consisting of silica cores and polymer coatings, either regular ("reference" fibers) or modified (by adding the NPM to the fiber coating).

- **Time-to-failure (TTF): delayed fracture**

  In this experiment, we applied mechanical stresses to the fiber specimens ("two-point bending" condition [36]) and measured the time-to-failure (TTF) for each case under two relative humidity (RH) conditions—RH = 35% ("normal") and RH = 100%. All the specimens were subjected to the predetermined humidity for at least 48 hours.

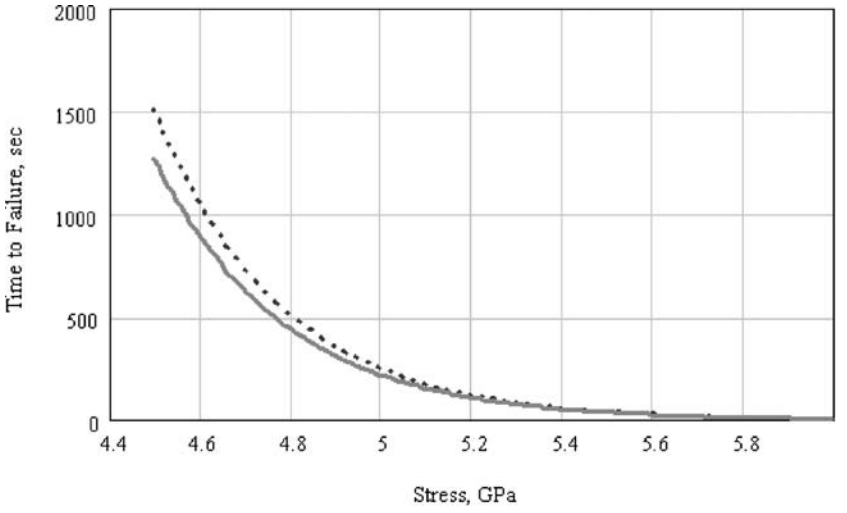

FIGURE 17.11. Time-to-failure vs. bending stress (35%RH). NPM-based sample (dotted curve) and the reference samples strength (solid curve).

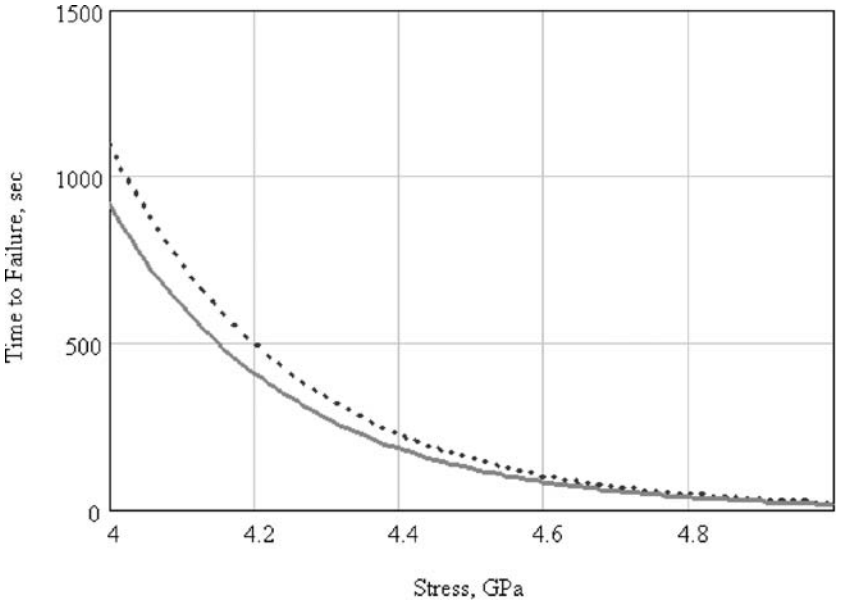

FIGURE 17.12. Time-to-failure vs. bending stress (100%RH). NPM-based sample (dotted curve) and the reference samples strength (solid curve).

- **Ultimate strength: "immediate" rupture**

  This experiment was carried out under the same RH and loading conditions as the previous ones, but the applied stress being such as to cause "immediate" rupture. The faceplates were brought together at the rate of 50 microns/sec up to the very moment of rupture.

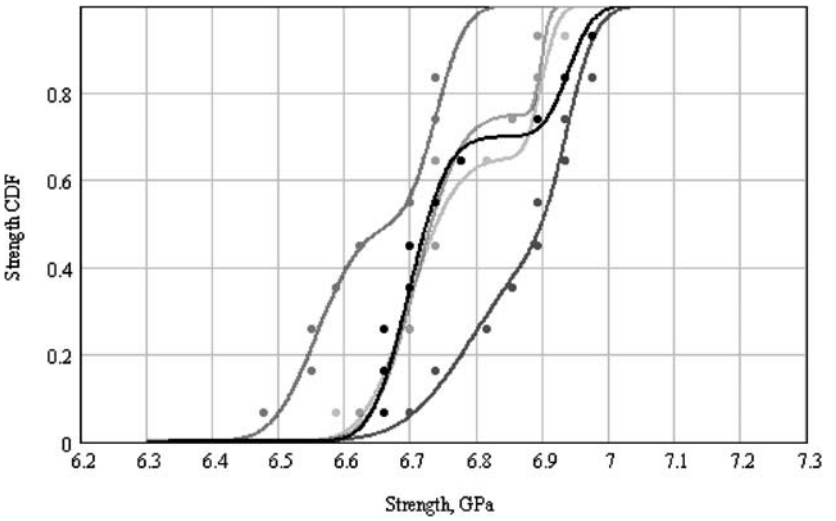

FIGURE 17.13. Strength probability for all tested at 35%RH samples.

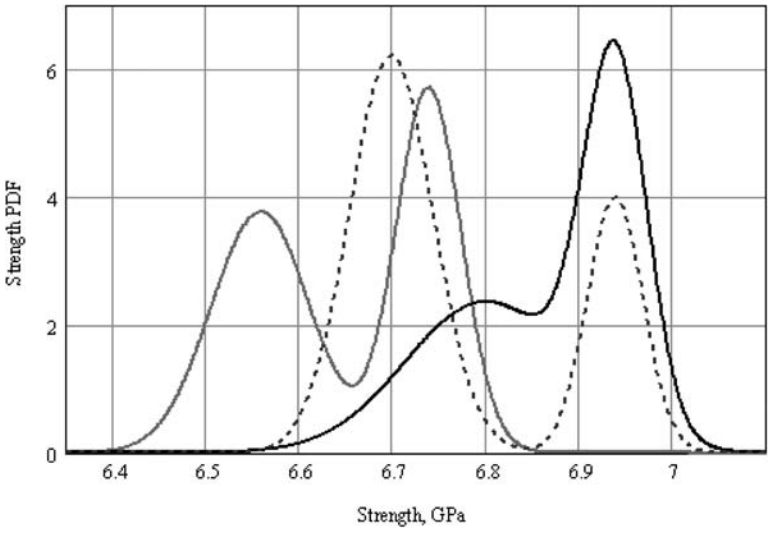

FIGURE 17.14. Strength PDF for samples tested at 35%RH.

In order to compare the TTF for different specimens, we approximated the relationships between the TTF and the applied stress, x, by a power law:

$$\mathrm{TTF}(x) = \frac{\tau}{x^n},$$

where τ is an empirical constant, representing the time to failure (rupture) under a unity stress level, and n is an empirical (material's)exponent. This relationship is shown for the two types of specimens in Figures 17.11 (35%RH) and 17.12 (100%RH). The obtained data clearly demonstrate the favorable effect of the NPM-based coating.

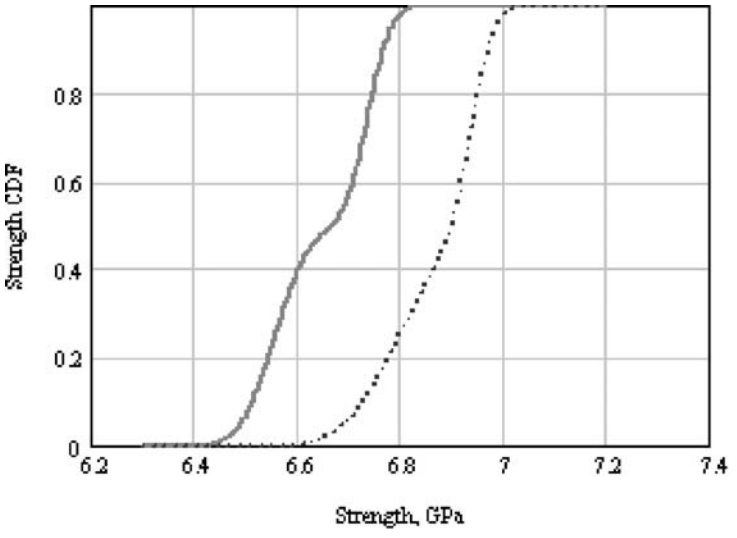

(a)

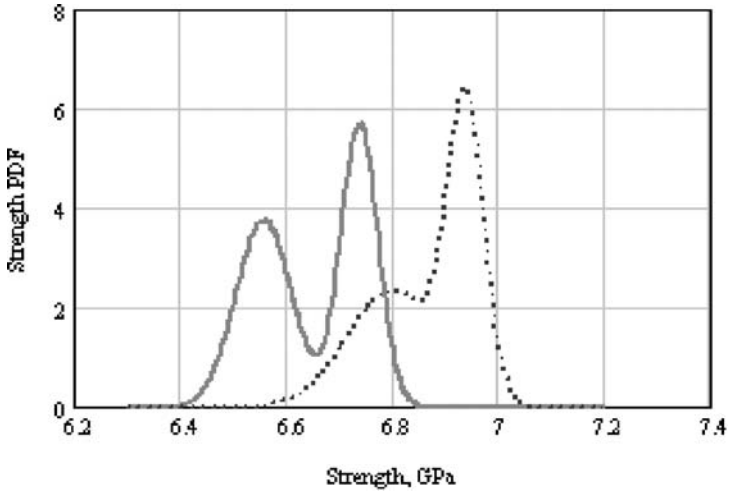

(b)

FIGURE 17.15. NPM-based sample (dotted curve) and the reference samples strength (solid curve) distributions—35%RH. (a) CDF, (b) PDF.

In order to analyze the results of the ultimate strength tests, the strength probability distributions (cumulative distribution functions, CDF) and their Weibull approximations [Equation (17.14)] were constructed for all the specimens (Figure 17.13). Figure 17.14 represents the derivatives of these functions, i.e., the probability density functions (PDF) for the fiber strength. Note that all the plots exhibit the double-slope pattern mentioned above. It is easy to see two explicit extremes on the strength distributions—the most deteriorated strength population corresponds to the reference case (no NPM-based fibers), and the least deteriorated strength has been demonstrated by the sam-

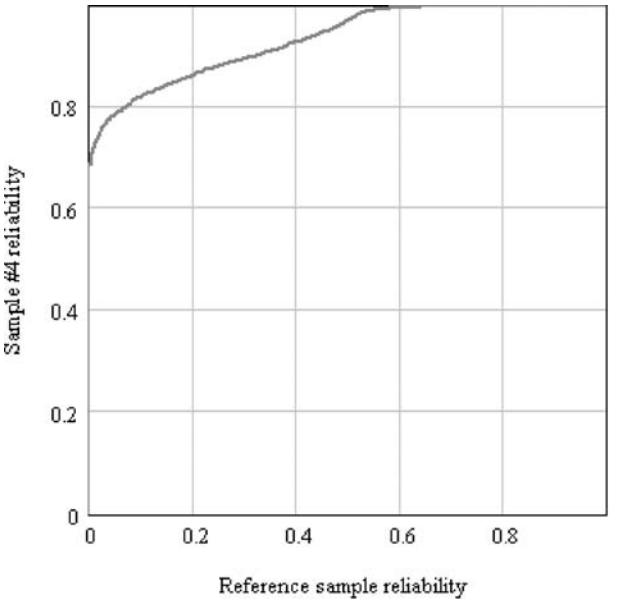

FIGURE 17.16. Reliability comparison—35%RH. NPM-based sample reliability vs. reference sample reliability.

ple with NPM containing coating. These two extreme cases are shown also in Figure 17.15.

The plot in Figure 17.16 demonstrates the reliability aspect of the differences in the strength distributions for the two extreme cases under the action of the same stress. The reliability range of the reference case is zero up to about 0.55, while the NPM-based case begins at about 0.7 and ends very close to 1, a fact which speaks for itself. The two cases demonstrated considerably the different mechanical and environmental performance, although the specimens were taken out of the same preform with the same core material, manufactured at the same drawing facility under identical conditions, and tested at the same time and at the same "age," by the same testing equipment and the same personnel. The improvements can be explained, first of all, by the "curing" abilities of the thixotropic NPM compound and the NPM-based coating. In addition, the coating, when subjected to bending deformations, has the ability to "slide" along the silica surface. This have to a situation, when the silica fiber and its coating behave (mechanically) "independently". This advantage was, in effect, anticipated in the basic considerations underlying the introduction of the NPM-based coating.

Figure 17.17 shows the strength and the reliability characteristics of the two cases at 100%RH. Unlike the 35% tests, where the undamaged and damaged subpopulations are divided almost evenly, the situation here is different. The NPM case exhibits the same proportion between the subpopulations—the point, at which the curve changes its shape, falls in the vicinity of 6 GPa, corresponding to the 0.5 probability. By contrast, for the reference case, this point falls at approximately 6.05 GPa, which corresponds to the probability of almost 90%, indicating that almost 90% of the reference population is damaged. The reference distribution is shifted considerably to the left (in the direction of lower strengths) in comparison with the NPM case. The maximum value of the right distribution for the ref-

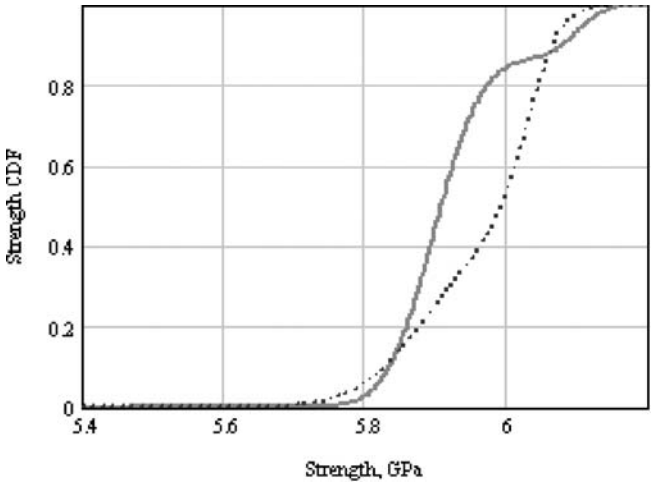

(a)

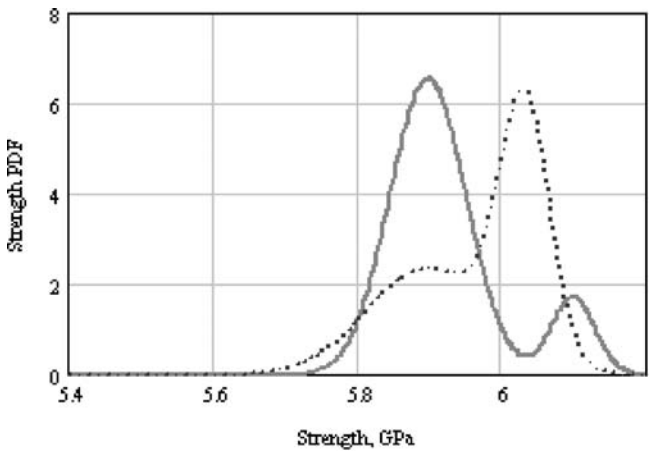

(b)

FIGURE 17.17. NPM-based sample (dotted curve) and the reference samples strength (solid curve) distributions—100%RH. (a) CDF, (b) PDF.

erence PDF covers a much smaller area than the high CDF values describing the damaged population.

The NPM sub-populations are separated less than those of the reference case. This indicates that in the NPM-based case we have both less damaged areas and a lesser damage (in the damaged specimens) than in the reference case. In the 35%RH test we observe, for the NPM case, much less damage and almost non-separated subpopulations. This subdivision most likely characterizes the micro-cracks and micro-damage of the core due to the manufacturing, winding and other fiber making processes. The healing action of the NPM slows down further deterioration of the fiber due to these defects, when in contact with water OH groups, and keeps the damaged population closer to the strength of the undamaged one. The reference case, therefore, represents growth of the damaged subpopulation for the

elevated humidity conditions, as well as the more strongly pronounced impact of damage on the specimen strength.

17.3. CONCLUSIONS

The following major conclusions can be drawn from the performed analysis:

- Application of the NPM results in substantial slowing-down of fiber aging and in the rate of damage accumulation;
- NPM is able to "heal" small core-surface defects;
- NPM effectively protects the silica surface from damage by water vapor;
- Application of the NPM improves substantially the fiber strength and reduces its variability;
- Application of the NPM coating is a promising way to improve optical, mechanical, environmental, reliability and even economic characteristics of silica light guides.

REFERENCES

1. E. Suhir, M. Fukuda, and C.R. Kurkjian, Eds., Reliability of photonic materials and structures, Materials Research Society Symposia Proceedings, Vol. 531, 1998.
2. D. Ingman and L.A. Reznik, Dynamic reliability model for damage Accumulation Processes, J. Nucl. Technol, 75, pp. 261–282 (1986).
3. D. Ingman and L.A. Reznik, Dynamic character of failure state in damage accumulation processes, Nuclear Science and Engineering, 107, pp. 284–290 (1991).
4. D. Ingman and L.A. Reznik, A dynamic model for element reliability, Nuclear Engineering and Design, 70, pp. 209–213 (1982).
5. K.K. Phani, Strength of long optical glass fibers, Journal of Applied Physics, 62, pp. 719–720 (1987).
6. D.S. Durham and W.J. Padgett, Cumulative damage models for system failure with application to carbon fibers and composites, Technometrics, 39, pp. 34–44 (1997).
7. H.M. Taylor, The Poisson-Weibull flaw model for brittle fiber strength, in J. Galambos, et al., Eds., Extreme Value Theory, Amsterdam, Kluwer, 1994, pp. 43–59.
8. M.I. Zeifman and D. Ingman, A dynamic view of strength bimodality of optical fibers, 2003.
9. A. Dumai, Reliability prediction on tensile loaded fiber optics, Research Thesis, Technion, 1991.
10. V.A. Petrov, A.Ya. Bashkarev, and V.I. Vettegren, Physical Basis of Durability Forecasting for Engineering Materials, Politekhnika, Sankt-Petersburg, 1993 (in Russian).
11. V.S. Kuksenko and V.P. Tamuz, Fracture Micromechanics of Polymer Materials, Martinus Nijhoff, Dordrecht, 1981.
12. M.I. Zeifman and D. Ingman, A percolation model for lifetime variability in polymeric materials under creep conditions, Journal of Applied Physics, 88, pp. 76–87 (2002).
13. M.I. Zeifman, A coarse semi-analytical lattice model of time-dependent failure of hierarchical materials, Europhysics Letters, 63, pp. 333–339 (2003).
14. G.P. Cherepanov, et al., Fractal fracture mechanics—a review, Engineering Fracture Mechanics, 51, pp. 997–1033 (1995).
15. B.S. Everitt and D.J. Hand, Finite Mixture Distributions, Chapmen and Hall, Cambridge, GB (1981).
16. D.B. Barker and Y. Yang, Effect of proof testing on optical fiber fusion splices, http://www.nepp.nasa.gov
17. P. Beumont and H. Sekine, Physical modelling of engineering problems of composites and structures, Applied Composite Materials, 7, pp. 13–37 (2000).
18. R.J. Castilone and T.A. Hanson, Strength and dynamic fatigue characteristic of aged fiber, Corning Inc., Corning, NY.
19. J.A. Collins, Failure of materials and Mechanical Design, 2nd edition, John Wiley&Sons, New York, 1981.
20. F. Desrumaux, F. Meraghni and M.L. Benzeggagh, Micromechanical modeling coupled to a reliability approach for damage evolution prediction in composite materials, Applied Composite Materials, 7, pp. 231–250 (2000).

21. X. Diao, A statistical equation of damage evolution, Engineering Fracture Mechanics, 52, pp. 33–42 (1995).
22. X. Diao and X. Xing, Nonequilibrium statistical theory of damage fracture for quasi-brittle materials, Engineering Fracture Mechanics, 56, pp. 321–330 (1997).
23. A. Ekberg, Fracture mechanics—some notes, http://www.solid.chalmers.se/~anek/research/fm.pdf.
24. M. Fukuda, Historical overview and future of optoelectronics reliability for optical fiber communication systems, Microelectronics Reliability, 40, pp. 27–35 (2000).
25. R. Ganesan, A stochastic modeling and analysis methodology for quantification of fatigue damage, Comput. Methods Appl. Mech. Engrg., 190, pp. 1005–1019 (2000).
26. G.S. Glasemann, The mechanical behavior of large flaws in optical fiber and their role in reliability prediction, Corning, New York. http://www.corning.com/opticalfiber/pdf/tr3268.pdf
27. W. Griffioen, et al., Evaluation of optical fiber lifetime models, Proc. SPIE, Vol. 1791, Optical Materials Reliability and Testing, 1992.
28. S.L. Semenov, Physical process determining strength and durability of optic fibers, Moscow, 1997.
29. D. Sauvage, D. Laffitte, J. Perinet, Ph. Berthier, and J.L. Gourdard, Reliability of optoelectronic components for telecommunications, Microelectronics Reliability, 40, pp. 1701–1708 (2000).
30. G.S. Wang, A probabilistic damage accumulation solution based on crack closure model, International Journal of Fatigue, 21, pp. 531–547 (1999).
31. D.S. Wilkinson, E. Maire, and R. Fougeres, A model for damage in a clustered particulate composite, Materials Science and Engineering, A262, pp. 264–270 (1999).
32. M.P. Wnuk, Constitutive modeling of damage accumulation and fracture in multiphase materials, Comput. Methods Appl. Mech. Engrg., 151, pp. 587–591 (1998).
33. J. Jireh, Yue Energy Concepts for Fracture, http://www.sv.vt.edu/classes/MSE2094_NoteBook/97ClassProj/anal/yue/energy.html
34. E. Suhir, Applied Probability for Engineers and Scientists, McGraw Hill, New York, 1997.
35. E. Suhir, Polymer coated optical glass fibers: review and extension, Proceedings of the POLYTRONIK'2003, Montreaux, October, 21–24, 1997.
36. E. Suhir, V. Ogenko, and D. Ingman, Two-point bending of coated optical fibers, Proceedings of the PhoMat'2003 Conference, San-Francisco, CA, August 2003.